

Event-based Sensing for Space Situational Awareness

Gregory Cohen, Saeed Afshar, and André van Schaik
The MARCS Institute for Brain, Behavior and Development
Western Sydney University, Sydney, Australia

Andrew Wabnitz, Travis Bessell, and Mark Rutten
National Security and Intelligence, Surveillance and Reconnaissance Division,
Defence Science and Technology Group

Brittany Morreale
United States Air Force

ABSTRACT

A revolutionary type of imaging device, known as a silicon retina or event-based sensor, has recently been developed and is gaining in popularity in the field of artificial vision systems. These devices are inspired by a biological retina and operate in a significantly different way to traditional CCD-based imaging sensors. While a CCD produces frames of pixel intensities, an event-based sensor produces a continuous stream of events, each of which is generated when a pixel detects a change in log light intensity. These pixels operate asynchronously and independently, producing an event-based output with high temporal resolution. There are also no fixed exposure times, allowing these devices to offer a very high dynamic range independently for each pixel. Additionally, these devices offer high-speed, low power operation and a sparse spatiotemporal output. As a consequence, the data from these sensors must be interpreted in a significantly different way to traditional imaging sensors and this paper explores the advantages this technology provides for space imaging.

The applicability and capabilities of event-based sensors for SSA applications are demonstrated through telescope field trials. Trial results have confirmed that the devices are capable of observing resident space objects from LEO through to GEO orbital regimes. Significantly, observations of RSOs were made during both day-time and night-time (terminator) conditions without modification to the camera or optics. The event based sensor's ability to image stars and satellites during day-time hours offers a dramatic capability increase for terrestrial optical sensors. This paper shows the field testing and validation of two different architectures of event-based imaging sensors. An event-based sensor's asynchronous output has an intrinsically low data-rate. In addition to low-bandwidth communications requirements, the low weight, low-power and high-speed make them ideally suitable to meeting the demanding challenges required by space-based SSA systems. Results from these experiments and the systems developed highlight the applicability of event-based sensors to ground and space-based SSA tasks.

1. INTRODUCTION

This work presents and demonstrates the viability and unique capabilities of a novel set of biologically-inspired camera technologies for applications in Space Situational Awareness (SSA). These cameras offer distinct advantages over conventional devices through a radically different operating paradigm, inspired by the functioning of biological retinas.

Biological vision systems are remarkably efficient, robust, and capable of operating over an incredible range of light intensities [1], and event-based cameras seek to replicate these advantages and the power efficiencies [2]. This paper focuses on the ability of these devices to perform space imaging tasks relative to terrestrial SSA, and does not explore their potential for use in low-power, bandwidth-constrained applications such as orbital platforms. These characteristics, however, make this technology extremely well suited to space-based applications.

This work represents the first instance of an event-based camera used for space imaging, and it was not clear at the outset how the sensors would perform under such conditions. Prior work with these sensors has been limited to toy problems [3], robotic-based navigation tasks [4], [5], fall detection [6], and classification tasks [7]. A few

researchers have experimented using event-based sensors on microscopes [8], and a number of researchers have investigated the application of these sensors in high-speed tracking applications [4], [9], [10]. Although these applications demonstrate interesting and exciting potential, the results achieved are often eclipsed by conventional approaches, which have benefitted from years of refinement and optimization.

By contrast, the application of event-based sensors for space imaging has already demonstrated unique capabilities arising from the nature of the hardware itself. It should be noted that these devices are still rudimentary prototypes which have not been optimized for any specific application. Future enhancements and optimization to these sensors should only serve to improve the results already achieved with the sensors used in the research.

2. NEUROMORPHIC VISION SENSORS

This work explores the use of a novel class of imaging devices known as silicon retinas for space situational awareness applications. These devices differ from conventional CCD cameras as they operate in an event-based paradigm, drawing inspiration from both the functioning of the biological retina and the computation and processing found in biological vision systems. The term neuromorphic engineering originally referred specifically to the development of electronic and silicon-based systems designed to replicate and mimic the behavior, structure, and organization of neuro-biological systems. The definition has since been expanded to include a range of biologically-inspired systems implemented using analogue, digital, and mixed-signal hardware [11]. Silicon retinas therefore comprise a neuromorphic approach to visual sensory transduction and seek to replicate the robustness, efficiency, and low power consumption of biological vision systems.

Silicon retinas operate in a vastly different paradigm from conventional imaging devices such as CCD sensors. Conventional cameras make use of a fixed-length and global exposure time to generate a frame of information at a regular time interval. These frames each contain data from every pixel and therefore tends to contain highly redundant information. Silicon retinas operate in a completely different and event-based paradigm, providing these sensors with advantages over conventional CCD sensors that are particularly well suited to space imaging tasks.

The pixels in these event-based cameras operate in an independent and asynchronous manner, producing data only in response to changes in the log intensity of the illumination at that pixel. The independent nature of each pixel removes the need for a global exposure time or shutter, allowing these devices to operate in a continuous fashion and diminishing the saturation effects suffered by conventional CCD devices. The asynchronous nature of the pixels produces a frame-free output with a high temporal resolution, serving to remove the effects of motion blur and providing the device with a very high dynamic range.

The output of both the ATIS and DAVIS camera can be viewed as a continuous stream of events e , each of which have the following form:

$$e = [x, y, p, t]^T$$

In which $\mathbf{u} = [x, y]$ denotes location of the pixel generating the event, $p \in \{-1, +1\}$ indicates the polarity of the change in illumination at the pixel causing the event, and t representing the time at which the event occurred. In a true event-based system, the time would be implicit as the arrival time of the event, but to preserve the timing when saving data from the camera, a time stamp is applied by the camera hardware as the event is generated. For both cameras, the timestamps are stored with microsecond resolution.

Although the first electronic models of the retina were developed in the 1970's [12], it was the integrated silicon retina by Mahowald and Mead [13] that represented the first viable imaging device in the 1980s. This device incorporated many of the characteristics found in the current generation of silicon retina. These characteristics include adaptive photoreceptors, spatial smoothing networks and an asynchronous communication paradigm.

This work focuses on two different neuromorphic event-based vision sensors, both deriving from the same original prototype 128 x 128 pixel sensor from Lichtsteiner, Posch and Delbruck [14]. These devices are the Dynamic and Active Vision Image Sensor (DAVIS) [15] and the Asynchronous Time-based Imaging Sensor (ATIS) [16]. Co-collects were performed using both sensors simultaneously, serving to further verify the results presented in this paper. Additionally, this work represents the first example of simultaneous and synchronized recordings from both cameras simultaneously.

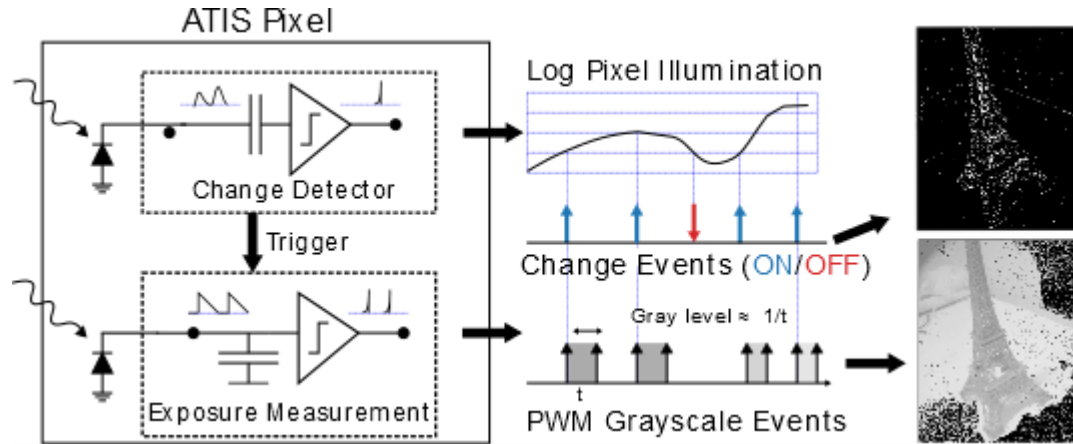


Figure 1: Diagram of the functioning of the ATIS pixel. Each pixel is capable of individually encoding change events and events containing illumination information. These events are generated and transmitted asynchronously from each pixel in the sensor. The above diagram shows the two components of each pixel in the ATIS sensor. These are the change detector circuitry and the exposure measurement circuitry. The DAVIS sensor implements the same change detection circuitry and system as shown in the ATIS diagram above. The ATIS sensor includes an additional asynchronous exposure measurement module capable of producing time-encoded measures of absolute illumination at each pixel. The DAVIS, by contrast, implements a different means of measuring absolute illumination through a process similar to that of a conventional frame-based camera.

The ATIS was developed by the Austrian Institute of Technology (AIT) and is now provided by the French company Chronocam¹. The ATIS offers a QVGA resolution of 305 × 240 pixels, each capable of operating independently and asynchronously. As shown in Figure 1, each pixel contains a level-crossing detector (TD) circuit and an exposure measurement circuit (EM) for absolute illumination measurements.

Fundamental to the differences between these sensors and conventional image sensors is the fact that these event-based imagers do not contain conventional analogue-to-digital converters (ADCs). These devices make use of threshold comparators to produce an encoded output in the form of asynchronous spikes in the Address-Event Representation (AER) [17]. For the TD circuitry, this takes the form of events generated with a polarity to indicate an increase or decrease in the relative illumination, and for the EM circuitry, the absolute illumination level determines the inter-spike interval between the two events generated by the exposure measurement circuitry on each pixel.

The DAVIS imager also offers dual outputs in the form of change detection and absolute pixel illumination measurement. The sensors are developed by the Institute of Neuroinformatics at the University of Zurich and commercialized by their spin-off company, iniLabs². The sensor is offered in various configurations, with both the original 128 x 128 pixel DVS and the 240 x 180 DAVIS cameras readily available. Higher resolution sensors (such as the 640 x 480 pixel device) are currently being prototyped and will be ready for production in the near future.

Table 1 provides the physical properties and characteristics of four different event-based neuromorphic sensors. In addition to the ATIS and DAVIS devices, the table also includes the DVS imaging device which is the precursor to the DAVIS sensor. Comparing the DVS to the DAVIS sensor shows the improvements in pixel density, power consumption, and fill factor from generation to generation. The table also includes the specifications of the DAVIS640 sensor, which is currently available only as a prototype sensor but boasts the highest pixel count of all event-based sensors to date. The ATIS and DAVIS cameras are the most mature of the event-based devices, and are the most widely available and well represented devices in the literature.

¹ Chronocam's website is available at [http:// www.chronocam.com/](http://www.chronocam.com/)

² IniLabs website is available at <http://inilabs.com/>

Table 1: Characteristics and physical properties of the commonly used event-based neuromorphic sensors.

Parameter	DVS [18]	DAVIS [15]	ATIS [16]	DAVIS 640
Pixels	128 x 128	240 x 180 (DVS)	304 x 240 (DVS)	640 x 480 (DVS)
	DVS only	240 x 180 (APS)	304 x 240 (APS)	640 x 480 (APS)
Power consumption	24 mW	5mW–14mW	50mW–175mW	5mW–14mW*
Dynamic Range	120 dB	130 dB	125 dB	130 dB*
Chip Size	6mm x 6.3mm	5mm x 5mm	9.9mm x 8.2mm	13.3mm x 13.3mm
CMOS Technology	0.35 μ m 4M 2P	0.18 μ m 6M 1P	0.18 μ m 6M 1P	0.18 μ m 6M 1P
Fill factor	8.1%	22%	20% TD, 10% EM	22%
Pixel Size	0.35 μ m x 0.35 μ m	0.18 μ m x 0.18 μ m	0.30 μ m x 0.30 μ m	0.18 μ m x 0.18 μ m

* Estimated values. Device is still in a prototype stage and accurate measurements are not yet available.

Physically, the ATIS and DAVIS cameras differ in terms of the number of pixels in the array and the physical size of each pixel. This has a significant impact on the resolving power of these devices in space imaging applications, with the ATIS camera having a wider field of view but less pixels per unit sky. Functionally, the major differences between the two devices concern how they produce a representation of the absolute illumination in a visual scene. The DAVIS camera contains a synchronous frame-based pixel sensor in addition to the change detection circuitry, allowing for the output of conventional frames and making this output compatible with the majority of computer vision algorithms and techniques. Unfortunately, this imaging modality suffers from all the problems associated with conventional cameras and does not provide any benefits in space imaging applications.

The exposure measurement functionality of the ATIS camera is fundamentally different from the approaches taken by the DAVIS camera. The EM portion of the camera can be triggered such that every pixel begins a measurement at the same time, effectively taking a snapshot and creating a frame of information. Operating the camera in this manner makes full use of the massively parallel nature of the exposure measurement circuitry, causing the device to behave like a time-to-first-spike device. The ATIS allows for the EM circuit to be triggered by the Change Detection circuit, thereby resulting in EM readings generated only in response to changes in the scene. This provides a form of hardware level compression which allows for highly efficient scene encoding. This is most significant in slowly changing scenes, where most of the illumination on each pixel remains constant.

The EM detection circuitry offers some interesting possibilities for space observation applications. Whereas this feature of the ATIS camera has historically seen very little use outside of purely visualization and calibration tasks, the technology may allow for unique sensing capabilities in SSA applications. The sensor can essentially be used as a time-to-first-spike imager, in which the entire pixel array begins integrating simultaneously, with the brightest pixels responding first.

3. EXPERIMENT SETUP

The experimental work performed with the ATIS and DAVIS cameras was undertaken at the DST Group's research facility for collaborative Space Situational Awareness experimentation. Located in Edinburgh, South Australia, the experiments made use of the robotic electro-optic telescope which was modified to support the event-based sensors and the existing astronomy equipment simultaneously.

The existing telescope configuration comprised an Officina Stellare RH200 telescope and an FLI Proline PL47010 camera. This telescope and camera was used to provide ground truth and to build an accurate mount model, allowing the event-based cameras to be accurately pointed at objects. The telescope is mounted on a Software Bisque Paramount MEII robotic mount, which was then augmented to support the event-based cameras as shown in Figure 2. The system is housed in a 7ft Aphelion Dome which also contains a PC that controls the robotic telescope and controls the event-based cameras.

The ATIS and DAVIS cameras were attached to an 8" Meade LX200 telescope as shown in Figure 2 (a). When performing co-collects with both event-based sensors, a second Meade LX200 was attached on the other side of the primary telescope as shown in (c). The field of view of the DAVIS sensor attached to the Meade telescope is 0.124° x 0.093° and the ATIS sensor is 0.261° x 0.206°.

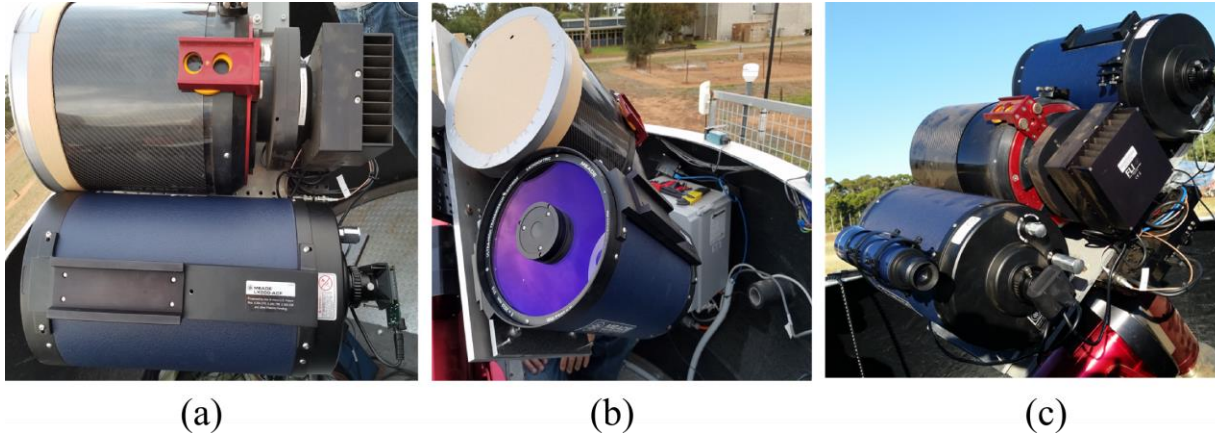


Figure 2: Photographs of the equipment used in the field trials for the event-based sensors. The above images show the telescopes used to test the event-based sensors. The event-based sensors were mounted alongside a conventional astronomy CCD camera (FLI Proline PL4710) as shown in (a) and bore-sighted to provide conventional images for ground truth comparisons. The ATIS camera can be seen attached to the base of the lower telescope in (a). Initial results were obtained using one event-based camera and the conventional CCD simultaneously as shown in (b). Note that the optics for the telescope for the event-based camera was not altered between daytime and nocturnal operations. A third configuration, shown in (c), contains two identical telescopes for the two event-based sensors whilst maintaining the conventional imaging camera in the center, allowing for simultaneous co-collects from both the ATIS and DAVIS cameras.

The telescopes were bore-sighted such that the overlapping fields of view of the telescopes were determined. The primary telescope and camera was then used to build an accurate mount model to compensate for the changes and modifications made to the telescopes when attaching sensors and telescopes.

The configuration shown in Figure 2 (b) also highlights an important point regarding the optics used for these experiments. The primary camera and telescope could not be used during daytime operation as the sensor would saturate. The event-based cameras can operate in both daytime and nocturnal conditions and required no alteration to the optics or the focus.

4. EVENT-BASED SPACE IMAGING

A significant portion of the contributions outlined in this work revolve around the mechanisms developed to detect and visualize data and objects of significance from the event-based cameras. The accurate pointing model available made it possible to position the field of view of the event-based cameras on objects of interest and to capture their results. Often it was not possible to directly observe the objects of interest from the raw data from the camera, nor from the rudimentary means of displaying the data that has been used in the past. As a result, the successful techniques developed to visualize and display the information are described below.

can be defined to assist in processing and visualizing the output of these event-based cameras. The first function P_e maps a polarity to a given spatial coordinate as follows:

$$\begin{aligned}
 P_e: \quad \mathbb{R} &\rightarrow \{-1, +1\} \\
 \mathbf{u}: \quad p &= P_e(\mathbf{u})
 \end{aligned}$$

The above function is useful in generating frames from event-based data, as plotting the function for each spatial coordinate provides a frame-like representation of the activity at the pixel. To generate event-based frames, P_e is

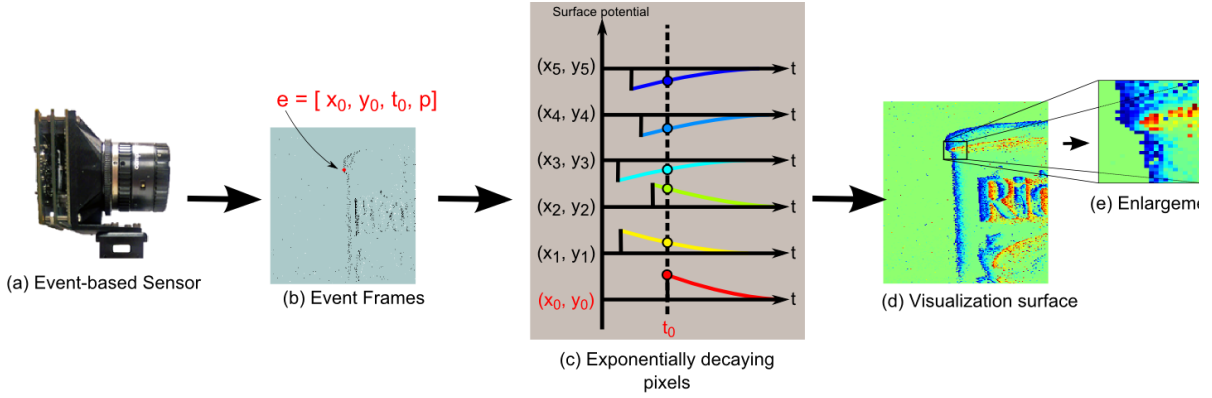


Figure 3: Visualization surfaces used to detect and track objects. The event-based output of the ATIS and DAVIS sensors are difficult to interpret as the data exists as a spatiotemporal pattern. Although frames can be rendered from the data by accumulating events over a fixed time window and then rendering them using the equation for P_e described in Section 4. An example of such an event-based frame is shown in (b) and can be misleading as it masks the temporal dynamics of the event-based data. Instead, a visualization technique based on fitting an exponentially decaying function to the last spike time for each pixel was developed, causing pixels that have fired more recently to assume a greater value, with the window of interest controlled by the rate of decay. This affects the slope of the decay at each pixel, as shown in (c), and serves to encode time as a continuous value in the display. The visualization, shown in (d), demonstrates how the colorization serves to highlight the pixels that have most recently displayed activity.

calculated over successive 40 ms windows, yielding the representation of the event-based data shown in Figure 3 (b).

In addition, a similar function Σ_e can be defined to map a time t to each spatial 2D coordinate as follows:

$$\begin{aligned} \Sigma_e: \quad \mathbb{R}^2 &\rightarrow \mathbb{R} \\ \mathbf{u}: \quad t &= \Sigma_e(\mathbf{u}) \end{aligned}$$

As time is a monotonically increasing function, the above function defines a monotonically increasing surface. This surface itself provides little benefit as it describes the last activity for each pixel. Through the applications of other functions to this surface, more descriptive and useful surfaces can be extracted that highlight or select other aspects of the event-based visual data. One such surface is the exponentially decaying surface defined as follows:

$$\Gamma_e(\mathbf{u}, t) = \begin{cases} p_e(\mathbf{u})e^{\left(\frac{\Sigma_e(\mathbf{u})-t}{\tau}\right)}, & \Sigma_e(\mathbf{u}) \leq t \\ 0, & \Sigma_e(\mathbf{u}) \geq t \end{cases}$$

The above function makes use of the two functions defined earlier to create an exponential decay based on a time constant defined by τ . This parameter defines the duration over which an event will influence the surface. In space imaging applications, this time constant is related to the speed taken for the slowest object of interest to pass across the field of view. An overview of this process is shown in Figure 3, in which the events from the ATIS camera are fitted with decaying exponential functions, as shown in (c), to yield a visualization surface encoding time since last event activity as a continuous variable. These surfaces are referred to as memory or visualization surfaces and are shown in (d) and (e) of Figure 3.

Finally, we can define a modified version of this surface that incorporates the residual value of the previous surface as follows:

$$\Phi_e(\mathbf{u}, t) = \begin{cases} (\Phi_e(\mathbf{u}, \tau_e) + p_e(\mathbf{u}))e^{\left(\frac{\Sigma_e(\mathbf{u})-t}{\tau}\right)}, & \Sigma_e(\mathbf{u}) \leq t \\ 0, & \Sigma_e(\mathbf{u}) \geq t \end{cases}$$

where τ_e denotes the time of arrival of the last event from any pixel on the array. Whereas the range of the exponentially decaying surface is Γ_e is bounded by $[-1, +1]$ as $\Sigma_e(\mathbf{u}) \leq t$, the range of the residual accumulating surface Φ_e is unbounded. This is the most commonly used visualization surface in this work, and a $\tau = 10^6 \mu\text{s}$ can be assumed if not otherwise specified.

5. RESULTS

5.1 Celestial Observations with event-based cameras

We have conducted five sets of telescope trials using event-based sensors at the DST Group site in Edinburgh, South Australia. The initial experiments focused on the successful attachment and integration of the event-based sensors into the existing robotic telescope configuration. For these experiments, only a single event-based sensor was attached at a time. Procedures for bore-sighting, focusing, and calibrating the event-based sensors were developed and the initial set of experiments proved the viability of event-based sensors for space-based sensors.

Figure 4 provides a set of examples of night-time observations of various celestial objects taken during the first sets of experiments. The figure shows the visualization surfaces described in the previous section at an instance in time. It is important to note that the data from the cameras comprises a continuous stream of data, and that the presence of objects is far easier to discern when watching the data live or in video form.

The recordings of Jupiter in (a) demonstrate the different fields of view between the two event-based sensors, as only one moon is visible in the DAVIS recording and at least three are visible in the ATIS recording. This recording was taken with the telescope set to sidereally track Jupiter, which results in the ring-like shape visible in both recordings. The internal portion of the planet appears more uniformly on the affected pixels and produces far fewer events than the outer edge. As a result, the changes on the outer ring appear far more prominently.

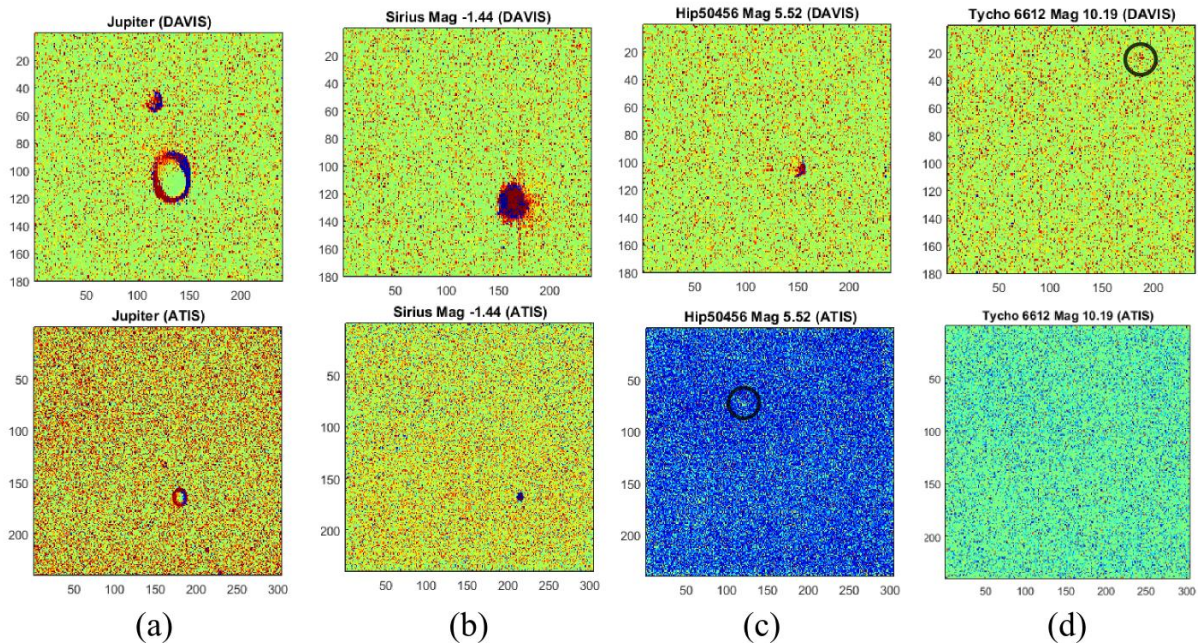


Figure 4: Examples of initial observations using the ATIS and DAVIS event-based cameras. The above images show visualization surfaces of varying objects captured with the ATIS and the DAVIS sensors during the initial sets of experiments. As the output of these cameras is a continuous stream, the presence of these objects is far more apparent when watching the output live or as a video. As a result, the figure has been annotated in places to show where the object is visible.

Examples of observations of stars are shown in the remainder of the figure. Sirius is shown in (b) and is clearly visible due to its high magnitude brightness. It is also clearly visible on the ATIS output, albeit far smaller. When moving to dimmer stars, such as shown in (c), it becomes increasingly difficult to see the star on the ATIS output. For the case of HIP 50456, it is clearly visible in the video of the data and the image has been annotated to assist the reader in finding the object. Finally, the magnitude 10.19 star show in (d) is still visible on the DAVIS sensor but is not visible on the ATIS sensor. It can be detected through post-processing, and is more easily spotted if the telescope is moving across it.

5.2 Nocturnal Detection of LEOs with an Event-Based Camera

Experiments to detect objects in low earth orbit were undertaken using the same configuration used in the initial experiments. The first experiments sought to prove that it was indeed possible to capture a LEO with an event-based camera and made use of the mount model and the NORAD catalogue to track a known object in LEO and recording with the event-based cameras.

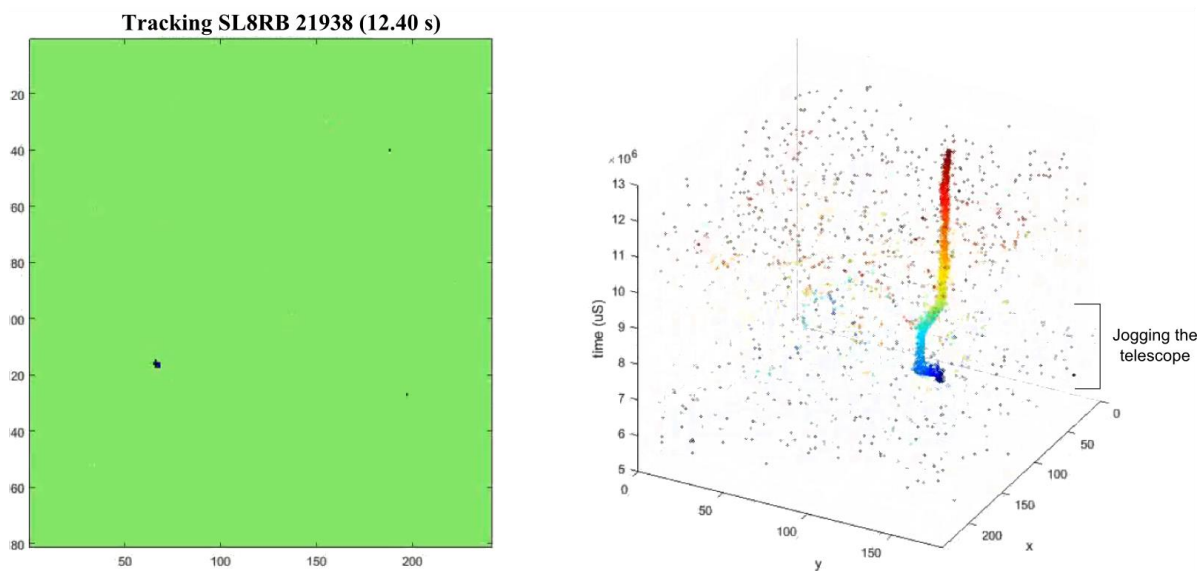


Figure 5: Results from recording a LEO, SL8RB (21938) whilst tracking. The above plot shows the results of capturing a tracked LEO using the DAVIS camera. Tracking the LEO was accomplished using the mount-model and the published TLE for the object and was visually confirmed using the CCD camera. The right-hand side figure shows a snapshot of the visualization surface for the tracked object. The plot on the left shows a representation of the events generated by the camera with time displayed in μs on the z-axis. Note that the tracking was jogged to check that the object was in the field of view, and this is clearly visible by the deviation in the tracked object present toward the start of the recording. The above recording was captured during night time, but similar results have since been obtained during daytime with both the ATIS and DAVIS sensors.

Tests were conducted with both the ATIS and DAVIS sensors and demonstrated that it was possible to visualize the objects during both daytime and night-time recordings. An example of the tracking of the LEO SL8RB (21938) at night with the DAVIS sensor is shown in Figure 5. As the object is being tracked, it remains in the field of view of the camera and is clearly visible on the visualization surface shown on the right-hand plot. The figure also shows a rendering of the events from the camera as a function of time, and demonstrates the continual and temporal nature of the output of these devices. Note that the colors in the above plots are used primarily to assist in rendering the trajectory. Once the object was acquired and confirmed on the CCD sensor, the telescope was jogged to assist in locating the object on the DAVIS sensor, the action of this jogging is clearly visible as the visible kink in the trajectory.

As the event-based cameras proved capable of producing meaningful data whilst actively tracking a LEO, the second set of experiment sought to catch a LEO moving through the field of view whilst stationary or siderally

tracking. This task is somewhat more challenging due to the very narrow fields of view of the event based cameras and the fact that the mount model was calibrated for the primary telescope and not the adjacent telescopes on which the event-based sensors were attached. As a result, the objects are only in the field of view for a very short space of time.

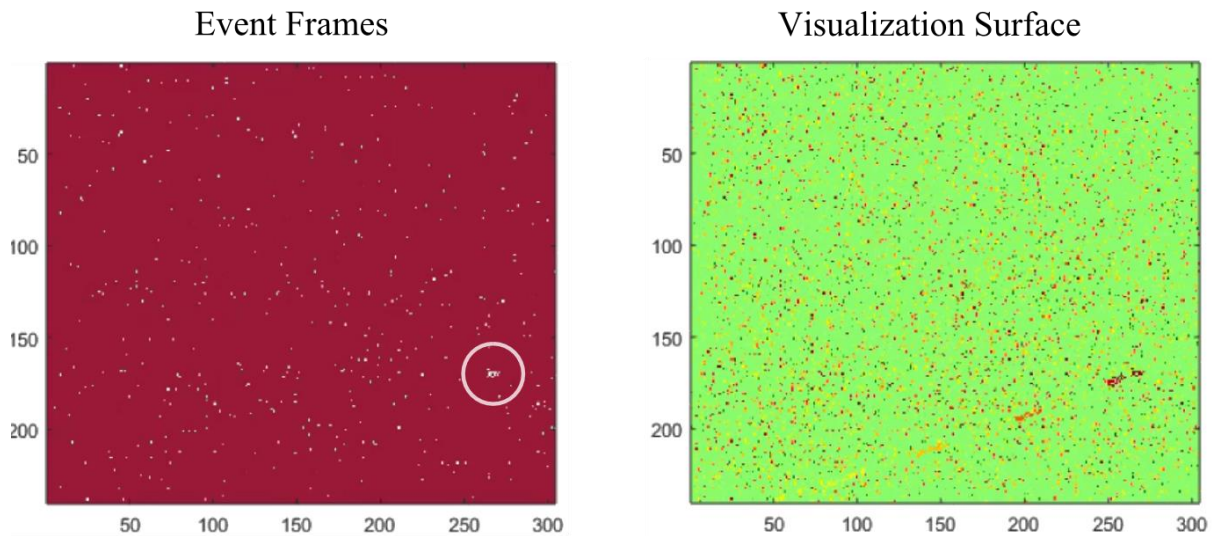


Figure 6: Detection of LEOs at night using the ATIS camera. The above figure shows the output from the ATIS camera whilst staring without any sidereal tracking. The plot shows the event frames on the left with the LEO circled for clarity. The frame in the above image represents a 40 ms region of the recording. A visualization surface is shown on the right-hand side which highlights the activity over the past 1 second using a sharp decaying exponential function with a $\tau = 1$ second. The path and trajectory of the object are clearly visible in the lower portion of the right plot. It is possible that the gaps in the trajectory are the results of glinting as the object rotates.

Successful detections of LEOs during night-time trials were obtained with both the ATIS and DAVIS cameras and an example is shown in Figure 6. The recording was performed using the ATIS camera, which benefits from the much wider field of view. The figure shows the event frame output of the camera on the right side of the image. The passage of the object across the field of view is far easier to discern in the live data or a video, and the object has been circled in the image.

The visualization surface is shown on the right-hand side of the image and highlights the use and importance of this visualization technique. As the surface preserves and highlights events that have occurred over a time period defined by the parameter τ (set to $1 \times 10^6 \mu s$ in the above figure), it captures the trajectory of the object as it crosses the field of view. This manifests as the trail visible on the surface, ending where at the current location of the object. Note that the gaps in the trajectory visible in this recording are not always present and may be an artefact of glinting. The continuous nature of these recording and the high temporal resolution provided by the sensor offer unique capabilities for measuring and characterizing these objects in real-time.

5.3 Nocturnal Recordings of Objects in Geosynchronous Orbit

The abilities for these event-based sensors to observe objects in geosynchronous orbit was also evaluated through a separate set of experiments. At present, observations of geosynchronous satellites have only been successfully at night, although practical and weather effects have limited opportunities for daytime exploration of the geo-belt with the event-based sensors. The ability to provide real-time and continuous imaging of geosynchronous objects with high temporal resolution is a particularly important task given the crowded nature of geo-belt.

Figure 7 shows a snapshot of the results of imaging a geosynchronous satellite, ABS-6 (25924), with the DAVIS camera at 2017/06/04 10:47:20 UTC from the testing site in Edinburgh, South Australia. As the event-based sensors report changes, which are primarily generated by movement or photometric effects, the process for imaging

geosynchronous objects is somewhat counter-intuitive. As geosynchronous objects are relatively stationary with respect to a point on the ground, it falls on a single point on the sensor and generates very few events. To compensate for this, the telescope can be moved to induce movement through ego-motion. This approach proved extremely effective, and the geosynchronous objects were detected by “leap-frogging” the geosynchronous object and then siderally tracking across it.

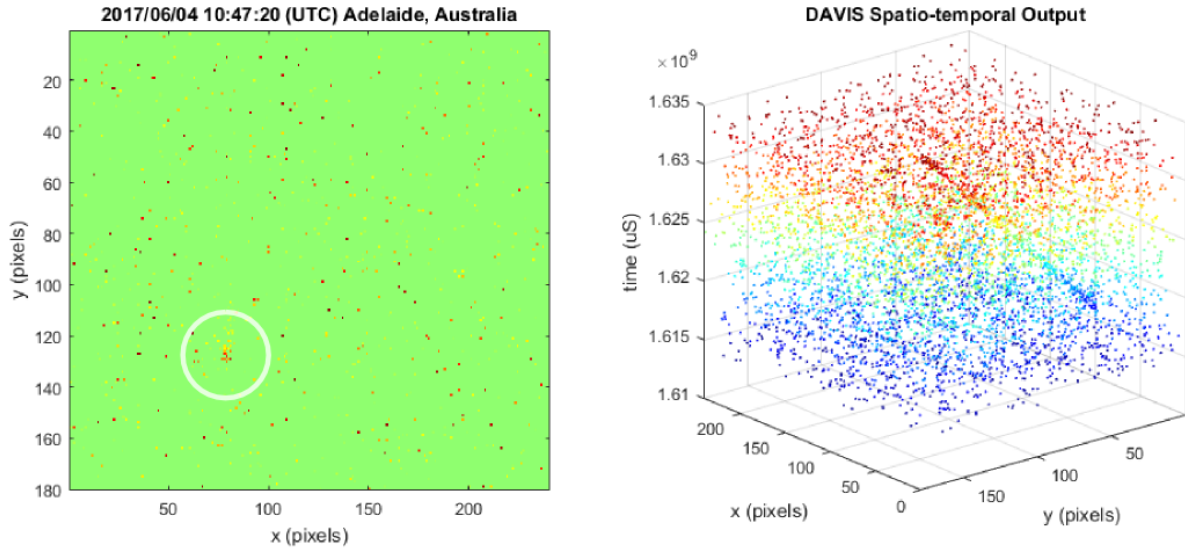


Figure 7: Plot of output from the event-based sensors from ABS-6 (25924) in geosynchronous orbit. The above graphs show the output from the DAVIS sensor whilst imaging the geosynchronous satellite ABS-6 (23924) at 2017/06/04 10:47:20 UTC from the DST Group SSA facility in Adelaide, Australia. The left-hand plot shows a visualization of the last 40 ms of data from the event-based sensor and provides a snapshot of the object (located within the white circle). It represents a snapshot of the output at the time indicated above the figure. The data from the camera is continuous and the figure on the right shows a plot of the output over time (displayed in μs). As the cameras are sensitive only to changes in the visual scene, the telescope needs to be siderally tracking in order to pick up the geosynchronous object, hence the satellite manifests as a continuous line with the slope determined by the rate of sidereal tracking. Note that the colors in both figures denote time and are were chosen primarily to highlight the trajectory of the object.

The figure shows the visualization surface on the left-hand side of the plot with the object indicated by a white circle. A plot of the object moving across the field of view as the telescope siderally tracks is shown on the right-hand side in a 3D plot with time as the z-axis. The slope of the trajectory is therefore the rate of sidereal tracking. These results confirm the viability of imaging geosynchronous objects with the event-based cameras and the continuous nature of the tracking and the high-temporal resolution of the output offer exciting potential for future work.

5.4 Daytime recordings of objects in Low Earth Orbit

Perhaps the most surprising results were obtained during daytime recordings with the ATIS and DAVIS sensors during which streaks through the visualization surfaces were observed whilst staring and siderally tracking known stars. The same streaks were observed in the absolute illumination output of the ATIS camera, which also preserves some trajectory information as absolute illumination updates are triggered by the change detection circuitry. These streaks were explored further through multiple experiments which captured multiple streaks during daylight hours on both the ATIS and DAVIS sensors.

Special software and real-time visualization techniques were built to assist in detecting and capturing these objects. Further refinements to the software included trajectory extraction and prediction. An example of the tracking and detection of LEO object during daylight hours is presented in Figure 8. The figure shows the results of a co-collect

from both the ATIS and DAVIS recordings simultaneously with the visualization surfaces shown at the top and the tracked trajectories of the objects passing through the field of view on the 3D plots presented below.

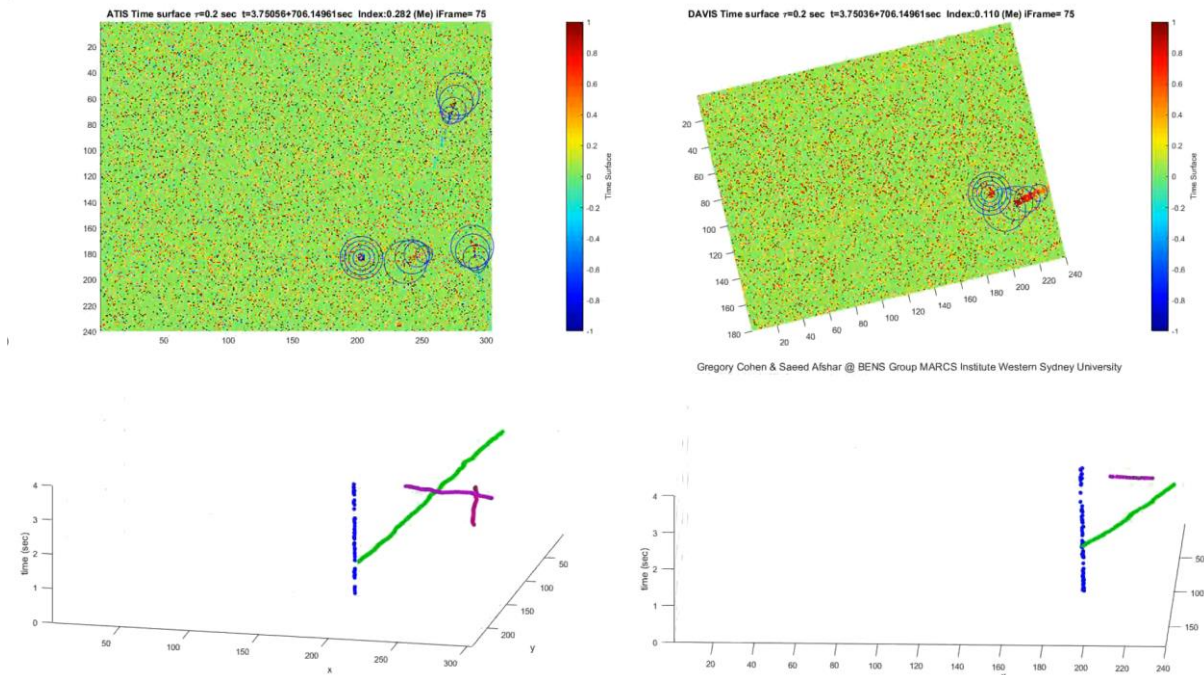


Figure 8: Co-collect of ATIS and DAVIS sensors in daytime detecting and tracking of LEOs. The above figure shows a combined plot of the output of the ATIS (left) and DAVIS (right) sensors collecting data during a co-collect daytime trial. The telescope was set to sidereally track Canopus to provide a fixed reference point (shown as the point surrounded by concentric circles in the top two blots and the vertical blue line of points in the bottom two plots). Note that the two sensors were not perfectly aligned, hence the rotation of the DAVIS output to allow the trajectories to match between the two plots. The top two plots show the visualization surfaces and the real-time tracking of objects of interest. Each object receives a set of concentric circles predicting the next possible location of the object, with the radius of the circle inversely proportional to the certainty of the prediction. Note that the same tracking mechanism is used to keep track of Canopus without any additional modification. The real-time locations of the object are tracked, with their trajectories displayed on the resulting 3D plots below. These plots show the pixel area of the sensor with time in seconds as the z-axis. The tracking mechanism is robust to objects that disappear and reappear within the visual scene and automatically detects and begins to track any new objects of interest. Note also that the field of view of the DAVIS camera is significantly smaller than that of the ATIS camera, and therefore it does not capture the same number of objects. The recordings were taken at 2017/06/04 06:03 UTC from the DST Group research facility in Adelaide.

The recordings from the two cameras are time-synchronized and the output from the DAVIS sensor has been rotated to allow the trajectories to match up in direction between the two visualization surfaces. This offset results from the bottom of the two sensors not being aligned properly. The conventional CCD camera could not be used during daylight operation and tracking relied primarily on the existing mount models.

The recordings were performed by pointing the telescopes at a known star to provide an accurate point of reference. The recordings shown in Figure 8 used Canopus as the reference star and it is visible in the center of the perfectly concentric circles in the upper plots and as the vertical trajectory shown in blue in the bottom plots.

The concentric circles visible in the image are a measure of tracking certainty, and are used to predict where the object will appear next with the probability decreasing in proportion to the radius of the circle. Detecting and tracking these objects is a complex task as their directions are not immediately obvious once they are detected,

requiring an orientation-invariant tracking system. Additionally, the objects disappear and re-appear as was observed in the night-time LEO recordings and the tracking mechanism needs to be invariant to such gaps.

Objects were detected on both cameras simultaneously, and through two different sets of optics, thus confirming that the objects are not an anomaly of the configuration. The telescopes were also focused for the far-field, and lower altitude objects such as birds and planes have been observed as clearly out of focus. The speed of the objects passing through the field of view also suggests that these objects are in LEO. Interestingly, these event-based cameras appear to be more effective at detecting low earth orbit objects in daylight than at night. This is possibly a result of their unique operating characteristics and the fact that daylight forces these devices to operate at the upper limits of their dynamic range, rather than the lower limits encountered when operating in dark conditions. As these devices are prototypes and are not cooled or optimized for low-light conditions, it is likely that their low-light performance can easily be improved by adopting the same techniques used to improve the accuracy on conventional CCD sensors.

6. CONCLUSIONS

This paper presents a novel approach to space imaging for space situational awareness using two different biologically-inspired cameras. Successful detection of objects in both LEO and GEO were demonstrated in both daylight and night-time conditions through co-collects involving multiple event-based sensors and a conventional CCD sensor for ground truth. The results demonstrate that the event-based cameras are capable of capturing objects of interest through a completely different event-based paradigm and with an unprecedented temporal resolution. As these sensors are non-cooled and unspecialized prototypes, these results represent baseline performance and all future efforts will lead to better results and capabilities.

7. REFERENCES

- [1] M. F. Land and R. D. Fernald, "The evolution of eyes.," *Annu. Rev. Neurosci.*, vol. 15, no. 1990, pp. 1–29, Jan. 1992.
- [2] T. Delbrück, B. Linares-Barranco, E. Culurciello, and C. Posch, "Activity-driven, event-based vision sensors," in *Proceedings of 2010 IEEE International Symposium on Circuits and Systems*, 2010, pp. 2426–2429.
- [3] T. Delbrück and M. Lang, "Robotic goalie with 3 ms reaction time at 40% CPU load using event-based dynamic vision sensor," *Front. Neurosci.*, vol. 7, no. 7 NOV, pp. 1–7, 2013.
- [4] E. Mueggler, B. Huber, and D. Scaramuzza, "Event-based, 6-DOF Pose Tracking for High-Speed Maneuvers," *Iros*, pp. 2761–2768, 2014.
- [5] B. Kueng, E. Mueggler, G. Gallego, and D. Scaramuzza, "Low-Latency Visual Odometry using Event-based Feature Tracks."
- [6] A. N. Belbachir, M. Litzenberger, S. Schraml, M. Hofstatter, D. Bauer, P. Schon, M. Humenberger, C. Sulzbachner, T. Lunden, and M. Merne, "CARE: A dynamic stereo vision sensor system for fall detection," in *2012 IEEE International Symposium on Circuits and Systems*, 2012, pp. 731–734.
- [7] G. K. Cohen, G. Orchard, S. Leng, J. Tapson, R. B. Benosman, and A. van Schaik, "Skimming Digits: Neuromorphic Classification of Spike-Encoded Images," *Front. Neurosci.*, vol. 10, no. 184, pp. 1–11, Apr. 2016.
- [8] Z. Ni, C. Pacoret, R. Benosman, S. H. Ieng, and S. Régnier, "Asynchronous Event Based High Speed Vision for Micro-particles Tracking," *J. Microsc.*, vol. 245, no. 3, pp. 236–244, 2011.
- [9] X. Lagorce, C. Meyer, S.-H. Ieng, D. Filliat, and R. Benosman, "Asynchronous Event-Based Multikernel Algorithm for High-Speed Visual Features Tracking.," *IEEE Trans. neural networks Learn. Syst.*, pp. 1–12, Sep. 2014.
- [10] Z. Ni, A. Bolopion, J. Agnus, R. Benosman, and S. Regnier, "Asynchronous Event-Based Visual Shape Tracking for Stable Haptic Feedback in Microrobotics," *IEEE Trans. Robot.*, vol. 28, no. 5, pp. 1081–1089, Oct. 2012.
- [11] G. Indiveri and T. K. Horiuchi, "Frontiers in neuromorphic engineering," *Frontiers in Neuroscience*, vol. 5, no. OCT, pp. 1–2, 2011.
- [12] K. Fukushima, Y. Yamaguchi, M. Yasuda, and S. Nagata, "An electronic model of the retina," *Proc. IEEE*, vol. 58, no. 12, pp. 1950–1952, 1970.
- [13] M. Mahowald, *An analog VLSI system for stereoscopic vision*. Kluwer Academic Publishers, 1994.

- [14] P. Lichtsteiner, C. Posch, and T. Delbrück, "A 128 X 128 120db 30mw asynchronous vision sensor that responds to relative intensity change," *2006 IEEE Int. Solid State Circuits Conf. - Dig. Tech. Pap.*, pp. 2004–2006, 2006.
- [15] C. Brandli, R. Berner, Minhao Yang, Shih-Chii Liu, and T. Delbruck, "A 240 x 180 130 dB 3 us Latency Global Shutter Spatiotemporal Vision Sensor," *IEEE J. Solid-State Circuits*, vol. 49, no. 10, pp. 2333–2341, Oct. 2014.
- [16] C. Posch, D. Matolin, and R. Wohlgenannt, "A QVGA 143 dB Dynamic Range Frame-Free PWM Image Sensor With Lossless Pixel-Level Video Compression and Time-Domain CDS," *IEEE J. Solid-State Circuits*, vol. 46, no. 1, pp. 259–275, Jan. 2011.
- [17] K. Boahen, "Point-to-point connectivity between neuromorphic chips using address events," *IEEE Trans. Circuits Syst. II Analog Digit. Signal Process.*, vol. 47, no. 5, pp. 416–434, May 2000.
- [18] P. Lichtsteiner, C. Posch, and T. Delbrück, "A 128 x 128 120 dB 15 us latency asynchronous temporal contrast vision sensor," *IEEE J. Solid-State Circuits*, vol. 43, no. 2, pp. 566–576, 2008.